Effects of Mn₁₋ₓZnₓFe₂O₄ Nanoparticles Concentration in a Silicone Matrix on Complex Permeability and Permittivity in the 1-10 GHz Range

Verônica C. S. Diniz[a]* , Antônio Carlos C. Migliano[b] , Ruth H. G. A. Kiminami[c],

Philippe E. de Medeiros[d] , Renalle C. A. de M. Nascimento[a] , Daniela de L. A. C. S. Andrade[a] ,

Ana C. F. M. Costa[e]

[a]Universidade Federal Rural de Pernambuco, Unidade Acadêmica do Cabo de Santo Agostinho, 54.518-430, Cabo de Santo Agostinho, PE, Brasil.
[b]Instituto de Pesquisas Avançadas, 12.228-00, São José dos Campos, SP, Brasil.
[c]Universidade Federal de São Carlos, Departamento de Engenharia de Materiais, 13.565-905, São Carlos, SP, Brasil.
[d]Universidade Federal do Rio Grande do Norte, Faculdade de Engenharia, Letras e Ciências Sociais do Seridó, 59.380-000, Rio Grande do Norte, RN, Brasil.
[e]Universidade Federal de Campina Grande, Unidade Acadêmica de Engenharia de Materiais, 58.429-900, Campina Grande, PB, Brasil.

Mn₁₋ₓZnₓFe₂O₄ ($0 \leq x \leq 0.65$) nanoferrite particles were used as filler in a silicone polymer matrix in order to obtain a composite material with the purpose of absorbing electromagnetic radiation. The composite was characterized by X-ray diffraction, transmission electron microscopy and force modulation microscopy (FMM) and the electromagnetic properties by means of network and impedance analyzers. It was observed that the composite with higher concentrations of Znₓ (x = 0.5 and 0.65) presented the lowest dispersion, due to the size of the zinc particles. This paper provides a framework for the practical application of absorbent composite materials of MnZn nanoferrite particles combined with silicone rubber to be used in 1-10 GHz frequency bands, with reflectivity values of -24 dB in the 6 GHz frequency range.

Keywords: electromagnetic absorption, nanoferrite particles, silicone rubber, composite materials.

1. Introduction

Spinel-type ferrites are ferromagnetic materials used in the field of magnetic materials due to their excellent electromagnetic properties. They can be applied in transformers[1-3], transmission devices[4-6], biomedical applications[7-11], for electromagnetic radiation absorption[12-15], among others.

These materials can be synthesized by different preparation methods, such as: conventional oxide blending[16-18], co-precipitation[19-21], sol-gel[22-24] and combustion[25-27]. However, low purity, heterogeneity, as well as aggregation are factors to be observed in the choice of the technique, especially in applications for electromagnetic absorption.

The combustion reaction technique has been standing out among the synthesis methods, since it is a safe, fast and relatively low-cost method, besides presenting adequate reproducibility for production of ceramic powders. Moreover, it is also able to produce objects with the desired structure and composition for a wide range of applications and still offers the possibility of large-scale production[28,29].

Electromagnetic radiation absorbing materials have attracted the attention of industry due to the growing demands of government legislation to control spurious electromagnetic radiation levels emitted by electronic equipment, that are associated with industrial standards for electromagnetic compatibility and interference. That study area has been reported by several authors[30-35].

The materials Electromagnetic radiation absorbing are composed of compounds that provide energy losses from electromagnetic radiation. In certain frequency ranges, these materials attenuate the incident electromagnetic radiation wave and dissipate the absorbed energy in the form of heat[36].

In order to supply the growing demand for electromagnetic absorbing films and coatings, composite materials consisting of ferrite particles embedded in polymeric matrices have been the subject of numerous researches[37-39]. Among these matrices we can highlight the silicone, which has very attractive original features in terms of optical and mechanical properties as well as good retention and flexibility, that are ideal for these applications[40].

The interest in polymer nanocomposites has rapidly been increasing in industry and in academia, due to their effect of altering many properties, such as absorbance, ion exchange capacity, thermal and solvent resistance, gas barrier properties, flame retardance, mechanical properties (hardness and stiffness) or simply to reduce the cost price[41]

*e-mail: veronica.diniz@ufrpe.br

Based on this context, this work aims to analyze the microstructural and electromagnetic properties of Mn-Zn ferrites incorporated in a silicone matrix for application as electromagnetic radiation absorbing materials. The absorption, permeability and permittivity properties were evaluated in the frequency range of 1-10 GHz, with ferrite nanoparticles of different granulometric bands dispersed in silicone rubber.

2. Experimental

2.1. Materials and methods

In order to carry out the synthesis of $Mn_{1-x}Zn_xFe_2O_4$ ferrites, with x = 0, 0.35, 0.5 and 0.65, high purity reagents (nitrates) were used, with glycerin being the fuel. The initial composition of the solution was based on the total valence of oxidizing and reducing reagents, using concepts from the propellants and explosives chemistry[42], with the purpose of establishing the stoichiometry of the interest phase. The redox mixture of metal nitrates and fuel was subjected to direct heating in a reactor with a production capacity of 200 g batches of product[43], illustrated in the Figure 1. The $Mn_{1-x}Zn_xFe_2O_4$ ferrite particles were dispersed in a silicone matrix in a mass ratio of 2:1.

2.2. Characterization

The samples were characterized by X-ray diffraction (XRD) on a Shimadzu XRD-6000 model diffractometer using a monochromatic radiation source (Cu-Kα of λ = 1.5418). Regarding the characterization of particle size distribution, a Horiba SZ-100 series zeta nanoparticle analyzer was used. The morphological aspects of the ferrite samples were analyzed

Figure 1. Redox mixture of metal nitrates and fuel on heating in the reactor.

using a Shimadzu Superscan SS-500 scanning electron microscope (SEM) and a Philips model EM420 transmission electron microscope (TEM), with a voltage of 120 kV. Each sample was analyzed by force modulation microscopy (FMM), with an atomic force microscope Agilent 5420 SPM. The electromagnetic evaluation was performed on an Agilent 4294A impedance analyzer by the SOL (Short-Open-Load) method, with the 85054D Agilent calibration kit, and on an Agilent Network Analyzer model N5231A, with the 85052D Agilent calibration kit, also by the SOL (Short-Open-Load) method[44], that uses short, open and load patterns.

3. Results and Discussion

3.1. X-ray diffraction (XRD)

Figure 2 illustrates the X-ray diffractograms of the pure $Mn_{1-x}Zn_xFe_2O_4$ (x = 0, 0.35, 0.5 and 0.65) ferrites obtained by large scale combustion reaction and when they are incorporated into silicone matrices. It can be seen from Figure 2 the formation of cubic inverse spinel phase of single $MnFe_2O_4$ ferrite and mixed Mn-Zn, which were identified by means of crystallographic records JCPDF 74-2403 and JCPDF 89-7556, respectively. All samples of pure ferrite showed peaks with high intensity and high basal width for all reflections, demonstrating their crystallinity and nanostructural characteristics. This indicates the efficiency of the combustion technique in making it possible to obtain these single-phase systems, with characteristics of nanoscale particles, in addition to the possibility of obtaining on a large scale.

Regarding the ferrites incorporated in the silicone matrix, a lower peak intensity was observed in relation to the ferrite of the single $MnFe_2O_4$ ferrite and mixed Mn-Zn. This behavior is probably associated with the presence of amorphous silicone rubber. However, its presence did not interfere with the formation of spinel structure of ferrites, as confirmed by the presence of characteristic peaks related to the cubic spinel phase.

Figure 3 illustrates Rietveld's refinement of $Mn_{1-x}Zn_xFe_2O_4$ (x = 0, 0.35, 0.5 and 0.65). The experimental points (blue points) were adjusted to intensity (red line) with the TOPAS program whose standard record is (ICDD 89-7554 for Mn-Zn ferrite and ICDD 74-2403 for $MnFe_2O_4$ ferrite).

Through the refinement data, it was possible to observe that the amounts of phases, for all samples obtained by large-scale combustion reaction, were 100%, so it can be concluded that presented a single phase, proving the results reported in theXRD analysis. The refined structural parameters and the factors related to progress, the quality of the refinement and the agreement between the observed and calculated profile, Rwp and GOF, are described in Table 1.

3.2. Particle size distribution

Figure 4 illustrates the diameter distribution of equivalent particles as a function of the cumulative volume of $Mn_{1-x}Zn_xFe_2O_4$ ferrites, with compositions x = 0, 0.35, 0.5 and 0.65, obtained by large scale combustion reaction in the range of 10 to 10.000 nm. The SZ-100 uses the light dynamic dispersion technique to determine particle size. Dynamic light scattering is the measurement of fluctuations
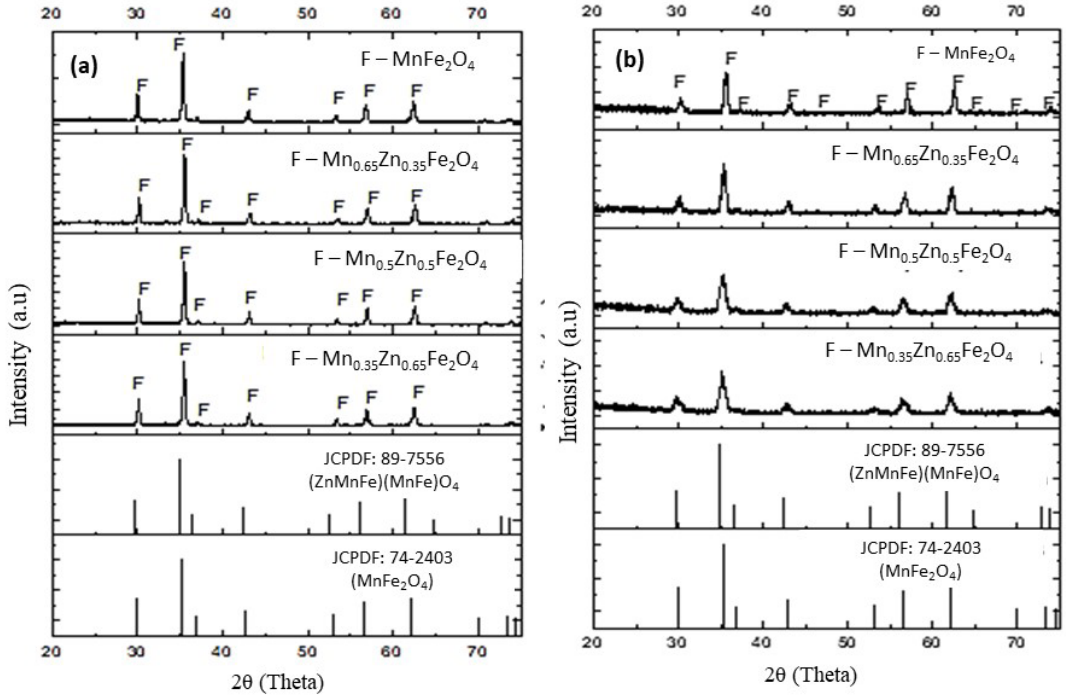
Effects of $Mn_{1-x}Zn_xFe_2O_4$ Nanoparticles Concentration in a Silicone Matrix on Complex Permeability and Permittivity in the 1-10 GHz Range

3

Figure 2. X-ray diffractograms of $Mn_{1-x}Zn_xFe_2O_4$ ferrite samples with compositions x = 0, 0.35, 0.5 and 0.65 (a) in powder and (b) inserted into the silicone.
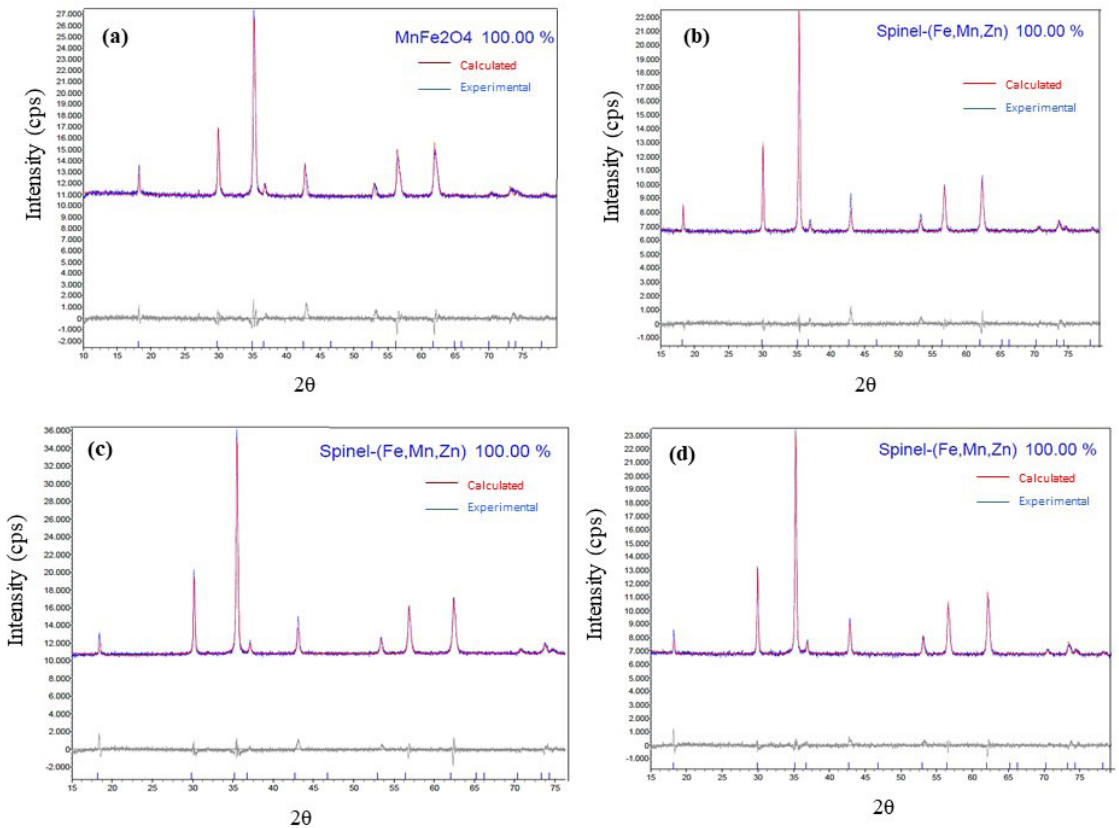

Figure 3. X-ray difratograms with Rietveld refinement with compositions (a) x = 0, (b) 0.35, (c) 0.5 and (d) 0.65.

Table 1. Rietveld refinement data of $Mn_{1-x}Zn_xFe_2O_4$ samples (x = 0, 0.35, 0.5 and 0.65).

Samples	R_{Wp}	Rexp	GOF	Phases (%)	Parameters of Network (Angstron)
$MnFe_2O_4$	1.67	0.94	11.76	$MnFe_2O_4$-100%	a=b=c=8.498
$Mn_{0.65}Zn_{0.35}Fe_2O_4$	1.61	1.21	1.33	(ZnMnFe)(MnFe)O_4 100%	a=b=c=8.497
$Mn_{0.5}Zn_{0.5}Fe_2O_4$	1.64	0.94	1.74	(ZnMnFe)(MnFe)O_4 100%	a=b=c=8.462
$Mn_{0.35}Zn_{0.65}Fe_2O_4$	1.65	1.18	1.39	(ZnMnFe)(MnFe)O_4 100%	a=b=c=8.455
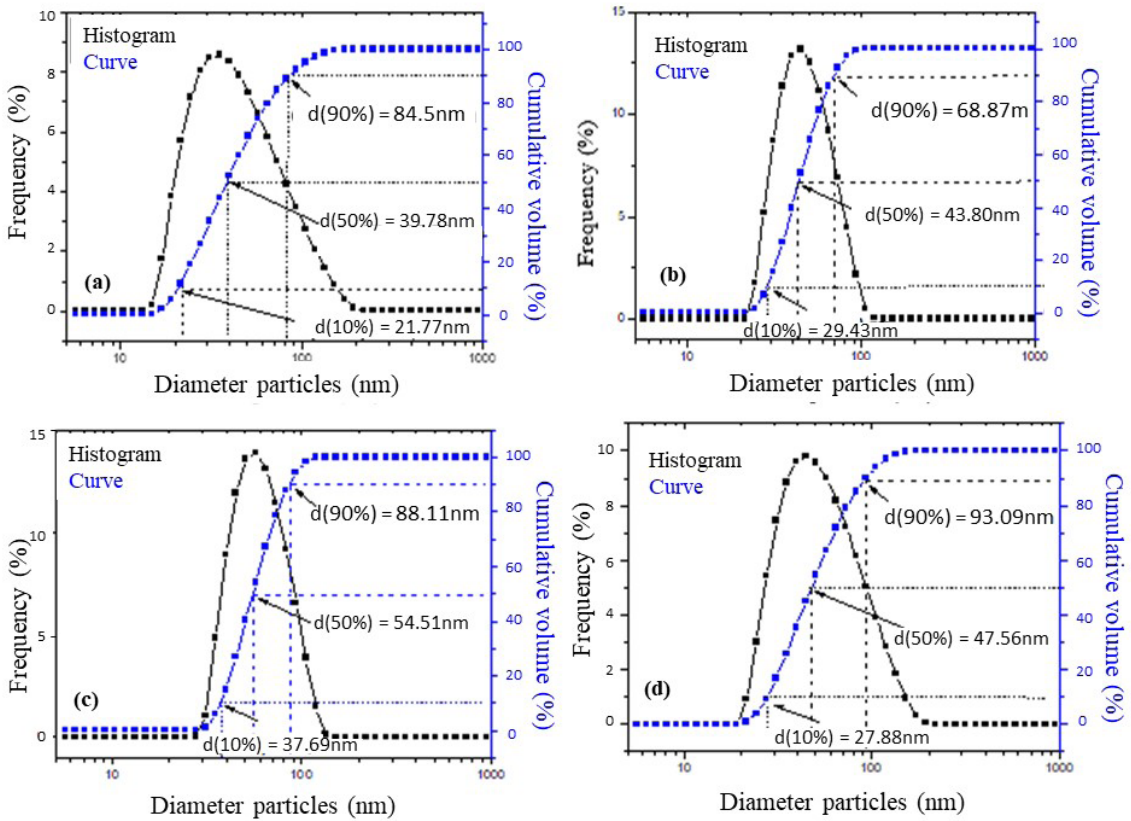
Figure 4. Particle size distribution of (a) $MnFe_2O_4$, (b) $Mn_{0.65}Zn_{0.35}Fe_2O4$, (c) $Mn_{0.5}Zn_{0.5}Fe_2O_4$ and (d) $Mn_{0.35}Zn_{0.65}Fe_2O_4$.

in the intensity of light dispersed over time. The reading occurs through the Brownian movement of the particles in an appropriate dispersant.

Considering the median diameter (50%), the sample $Mn_{0.5}Zn_{0.5}Fe_2O_4$ presented the largest particle size, with a value of 54.5 nm, which coincided with the narrower distribution curve, indicating the reduction of the average separation distance between the particles. The $MnFe_2O_4$ sample had the smallest median diameter (50%), with a value of 39.78 nm, and a wider distribution curve, which can be attributed to the fact that it is the only sample that does not have zinc in its composition.

3.3. Transmission electron microscopy (TEM)

Figure 5 illustrates the micrographs observed by Transmission Electron Microscopy (TEM) in a bright field and their respective refractive patterns of $Mn_{1-x}Zn_xFe_2O_4$ ferrites, with compositions x = 0, 0.35, 0.5 and 0.65, obtained by large scale combustion reaction. From the micrographs obtained by TEM, it was possible to observe, in general, the formation of agglomerates consisting of hexagonal and spherical shaped nanoparticles with varying sizes. It is possible to note that the sample for x = 0 had an average particle size of 75 ± 0.9 nm, for x = 0.35 it was 71.5 ± 0.4 nm, for x = 0.5 it was 78 ± 1.2 nm and for sample x = 0.65 it was 63 ± 0.5 nm. Overall,

Effects of $Mn_{1-x}Zn_xFe_2O_4$ Nanoparticles Concentration in a Silicone Matrix on Complex Permeability and Permittivity in the 1-10 GHz Range
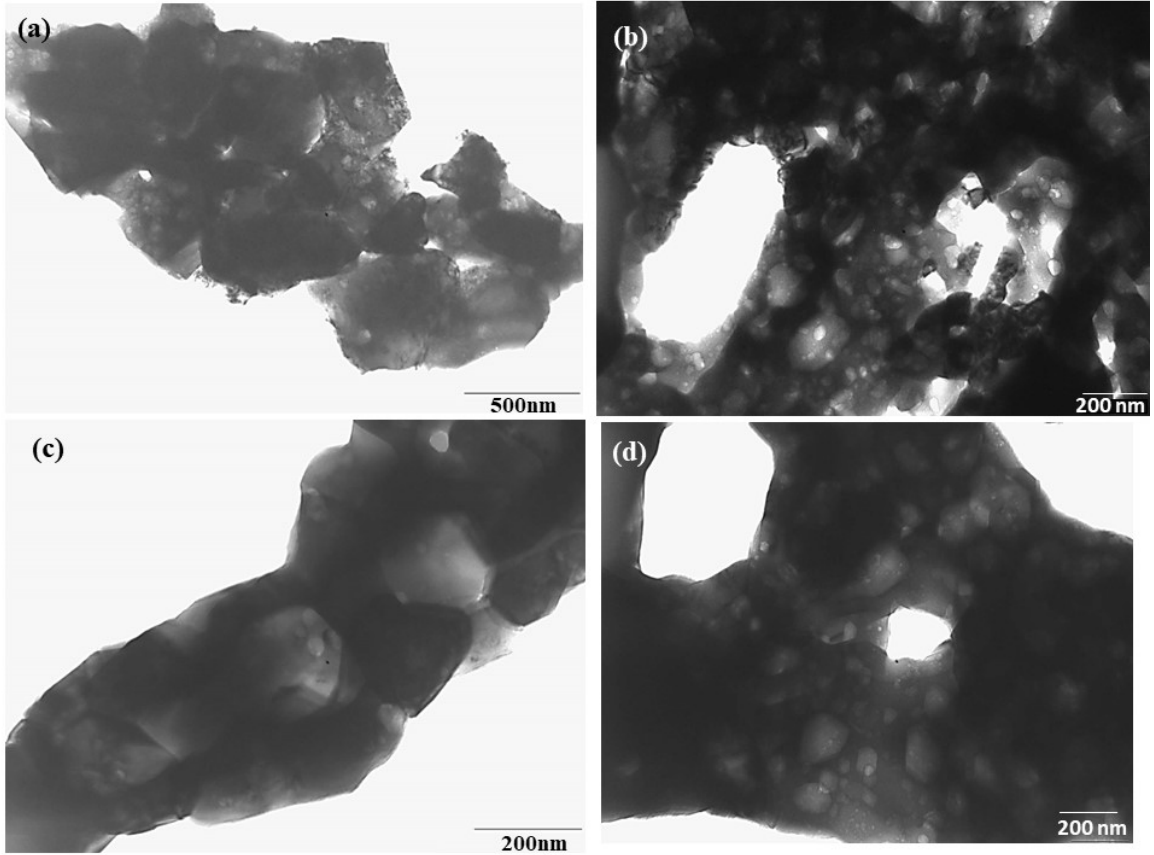
5

Figure 5. Micrographs obtained by TEM for the samples of (a) $MnFe_2O_4$, (b) $Mn_{0.65}Zn_{0.35}Fe_2O_4$, (c) $Mn_{0.5}Zn_{0.5}Fe_2O_4$ and (d) $Mn_{0.35}Zn_{0.65}Fe_2O_4$.

all the systems presented particle sizes less than 100 nm, indicating that they can be considered as materials with nanostructural characteristics. It was noted that besides the samples with x = 0 and x = 0.5 present a larger particle size, they also present an aspect of greater agglomeration, with the presence of grain outlines of the pre-sintered particles, which are highlighted in Figures 5a and 5c.

In relation to the increase in the zinc content in the composition, a non-linear behavior was observed, since as the zinc content of the sample $Mn_{0.65}Zn_{0.35}Fe_2O_4$ is added to $Mn_{0.5}Zn_{0.5}Fe_2O_4$ there was an increase of approximately 8% followed by a 20% decrease from the sample $Mn_{0.5}Zn_{0.5}Fe_2O_4$ to $Mn_{0.35}Zn_{0.65}Fe_2O_4$.

In the case of polycrystalline ferrites, the permittivity is a response attributed to the spaces between the loads at the grain boundaries, while the permeability is related to the magnetizing mechanisms: the spin rotations and the size of the magnetic domains, that is, the particle size[45].

3.4. Scanning electron microscopy (SEM)

Figure 6a-d illustrates the sample morphology of $Mn_{1-x}Zn_xFe_2O_4$ ferrites, with compositions x = 0, 0.35, 0.5 and 0.65, embedded in a silicone matrix. From the micrographs, it was possible to observe, in general, that the samples presented a uniform distribution of the ferrite load within the silicone matrix, however with the formation of irregularly

dispersed agglomerates throughout the matrix. There are no significant changes in the composite morphology with the change in compositions.

3.5. Force modulation microscopy (FMM)

Figure 7a-d shows the FMM oscillation phases of $Mn_{1-x}Zn_xFe_2O_4$ ferrites, with compositions x = 0, x= 0.35, x= 0.5 and x= 0.65, embedded in a silicone matrix. It is noted through the FMM that the increase in the Zn content provided less dispersion of the particles, which tended to agglomerate inside the composite, since Zn presents smaller particles in relation to Mn, and then promote a greater state of agglomeration mainly due to the mutual attraction of the nanoparticles[46]. However, one should point out that the oscillation phase of FMM is only a relative indicator of homogeneity, since it shows only the contrast between dispersion and particle agglomeration for each case, not being used as a comparison to calculate the average stiffness of each sample, for which the oscillation amplitude value is required.

3.6. Magnetic Permeability and magnetic permittivity

Figure 8 illustrates the measurements of complex real magnetic permeability (μ') e imaginary magnetic permeability (μ") versus frequency for $Mn_{1-x}Zn_xFe_2O_4$ ferrites, with
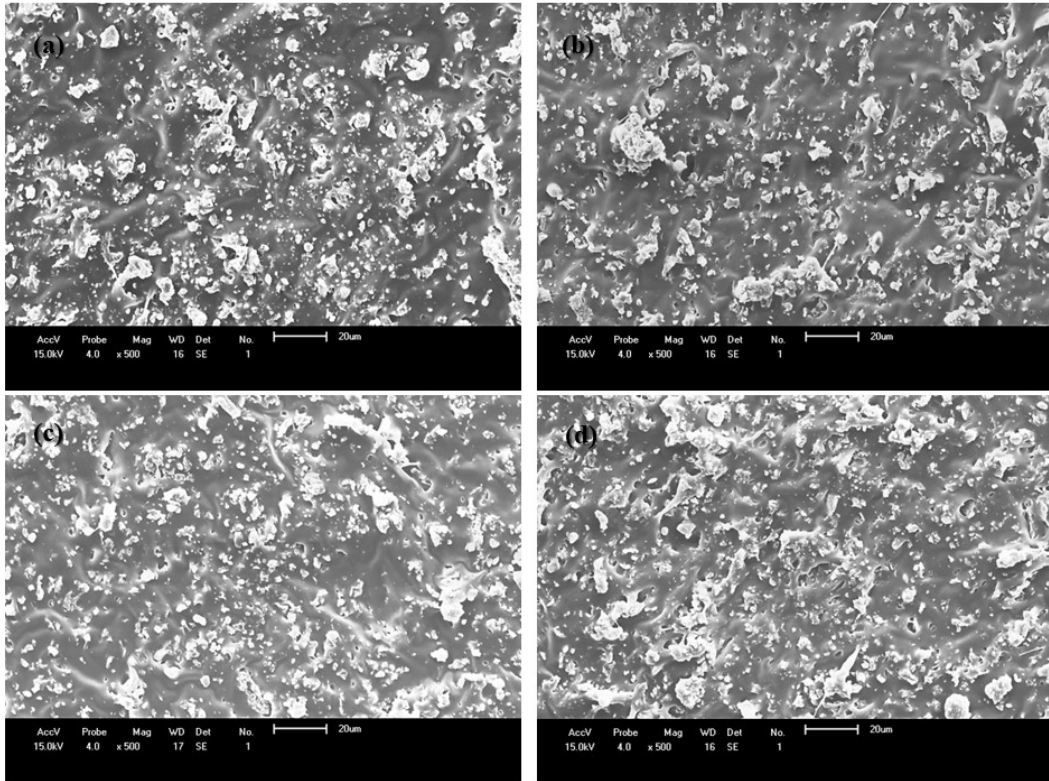
Figure 6. Morphological characteristics obtained by SEM for the samples of (a) $MnFe_2O_4$, (b) $Mn_{0.65}Zn_{0.35}Fe_2O_4$, (c) $Mn_{0.5}Zn_{0.5}Fe_2O_4$ e (d) $Mn_{0.35}Zn_{0.65}Fe_2O_4$ (2.000 increase).
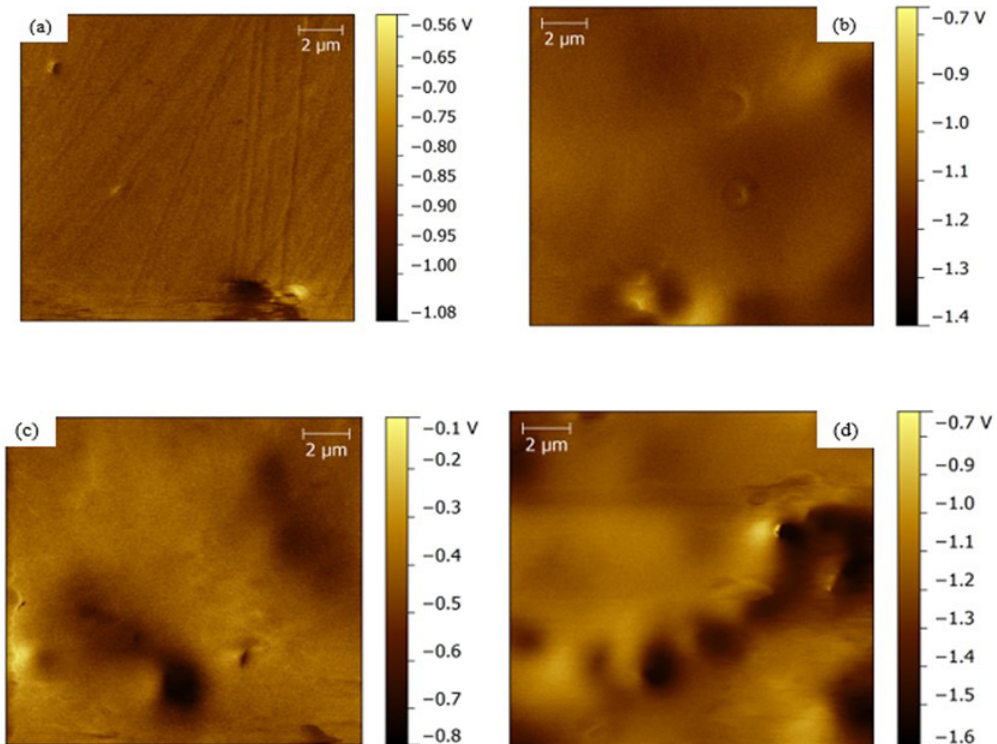
Figure 7. Phase angle of the FMM for the samples of (a) $MnFe_2O_4$, (b) $Mn_{0.65}Zn_{0.35}Fe_2O_4$, (c) $Mn_{0.5}Zn_{0.5}Fe_2O_4$ and (d) $Mn_{0.35}Zn_{0.65}Fe_2O_4$.

Effects of Mn$_{1-x}$Zn$_x$Fe$_2$O$_4$ Nanoparticles Concentration in a Silicone Matrix on Complex Permeability and Permittivity in the 1-10 GHz Range

7

compositions x = 0, 0.35, 0.5 and 0.65, embedded in a silicone matrix. The complex permeability spectra for all samples are plotted as a function of frequency. Both the real (μ') and the imaginary (μ") parts of the permeability were apparently constant and with close values (μr = 3.4) for the blankets with x = 0.5 and 0.0, respectively, in the frequency range 1 to 10 GHz. For blankets with x = 0.65 and 0.35, which has a lower concentration of Zn, the values were approximately μr = 2.7 and 2.9.

These responses of permeability as a function of increased frequency are attributed to the combinatorial magnetic relaxations of domain wall movements and spin rotations in the nanoferrites incorporated in the silicone. This finding is in accordance with several data reported in the literature[47-49].

Figure 9 illustrates that the permittivity versus Frequency for blankets with Mn$_{1-x}$Zn$_x$Fe$_2$O$_4$ ferrites with compositions x = 0, 0.35, 0.5 and 0.65.

This behavior is compatible with its real part (ε'), which remains very low across the measurement range for all investigated samples. The variation in the Zn concentration did not represent major distortions in the electrical values, which were around ε'= 1.2 for all samples but with a decay at high frequencies. The reduction of the permittivity value for materials at high frequencies can be justified mainly because of the atomic and electronic polarization within the ferrite nanoparticles. The electrical polarization mechanism is considered to be the cause of the jump of electrons between Fe^{2+} and Fe^{3+} at octahedral sites. According to Nasir et al.[50] it is known that polarization can be maintained due to the longer relaxation time at low frequencies, and not be maintained with increasing frequency, since the relaxation time decreases in greater frequency. This behavior has been reported by several authors[51,52].

According to transmission line theory, the reflection loss (RL) can be calculated from of the material impedance value, Z_{in}, and of the characteristic air impedance, Z_0. The material impedance is calculated based on the permittivity and complex relative permeability, according to Equation 1[53]:

$$Z_{in} = Z_0 \sqrt{\frac{\mu_r^*}{\varepsilon_r^*}} \tanh\left[j\left(\frac{\omega \cdot d}{c}\right) \sqrt{\mu_r^* \varepsilon_r^*} \right].$$

Thus, the reflectivity is calculated in decibels using Equation 2:

$$RL = 20\log_{10}\left| \frac{Z_{in} - Z_0}{Z_{in} + Z_0} \right|.$$

Figure 10 illustrates the loss of reflection (dB) for blankets of Mn$_{1-x}$Zn$_x$Fe$_2$O$_4$ composition, with x = 0, 0.35, 0.5 and 0.65, with a thickness of 20 mm. For obtaining an electromagnetic radiation absorbing material, the real part of the permeability must be maximized and the real part of the permittivity minimized, so that these parameters are close to each other to achieve harmonization conditions. From Figure 10 it can be seen that the blanket with equal concentrations of Zn and Mn presented the minimum reflection loss, which was -24 dB, at a frequency around 6 GHz. With x=0.35 in mass of ferrite in the absorbing material, the reflectivity is -10 dB at the frequency of 7 GHz. It was observed that the samples X= 0 and 0.5 showed similar reflectivity values in

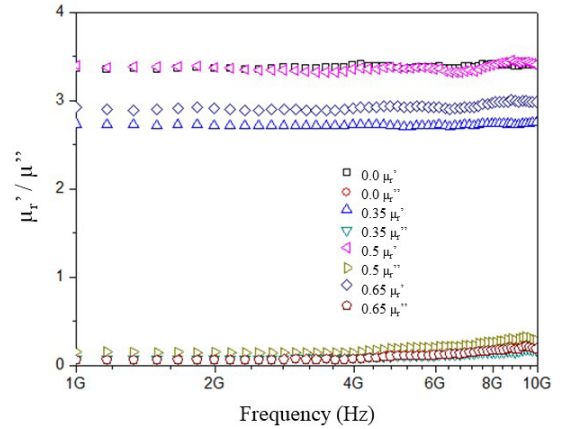the 6 GHz range, this can be justified by the fact that the samples present the larger particle sizes.

Figure 8. Permeability versus Frequency for the blankets with Mn$_{1-x}$Zn$_x$Fe$_2$O$_4$ ferrites with compositions x = 0, 0.35, 0.5 and 0.65.
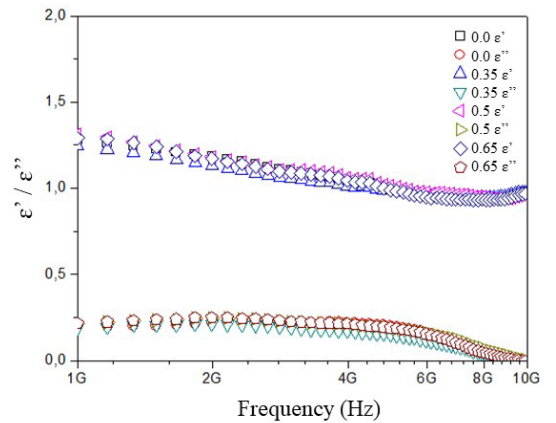

Figure 9. Permittivity versus Frequency for blankets with Mn$_{1-x}$Zn$_x$Fe$_2$O$_4$ ferrites with compositions x = 0, 0.35, 0.5 and 0.65.
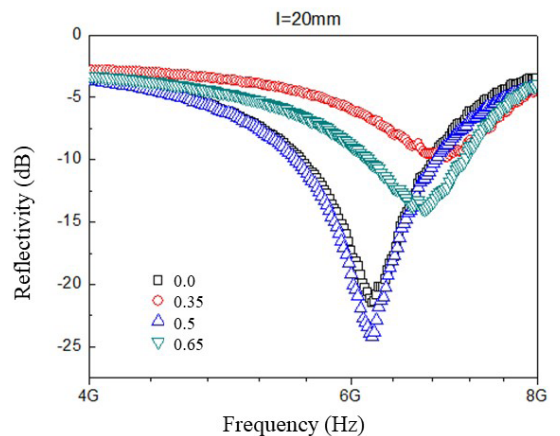

Figure 10. Blankets reflectivity with Mn$_{1-x}$Zn$_x$Fe$_2$O$_4$ ferrites with compositions x = 0, 0.35, 0.5 and 0.65.

The technique of phase cancellation of the electromagnetic wave seeks to adjust the thickness of the absorber, in order to cause the phase cancellation of the incident wave with those of the wave emerging from the absorber, at the interface of the absorber material with the air. This technique is widely used in the production of the resonant absorbers. Resonant absorbers represent the majority of the market. These absorbers perform relatively well, but are effective only in very narrow frequency ranges[54].

The high absorption of this sample is due to its permeability values of the real and imaginary parts, which were the highest in relation to the other compositions.

The data obtained show promising data to be used in the frequency range between 6 to 8Ghz, the composites obtained show promising data to be used in the camouflage of structures, in order not to occur detection by radars, in narrow band.

4. Conclusions

The synthesis by combustion reaction was a favorable technique for single-phase obtaining of $Mn_{1-x}Zn_xFe_2O_4$ (x = 0, 0.35, 0.5 and 0.65) ferrites on a large scale and with high crystallinity, without significant changes when incorporated into the silicone. The average particle sizes were around 45 nm. The blanket with the highest Zn concentrations (x = 0.5 and 0.65) presented the lowest dispersion, due to the smaller zinc particles, which ended up promoting a high state of agglomeration. Regarding the absorptive character of the blankets, the composition x = 0.5 presented the reflectivity value of -24dB in the 6 GHz frequency range. From the results obtained, it is important to highlight how promising is the incorporation of nanoparticles into polymeric blankets, being possible to achieve optimal absorption values which allows its application, for example, in the camouflage of structures, in order not to occur the detection by radars, in narrow band.

From these results it is possible to manage the obtaining of hybrid absorbers, by combining magnetic additives with different concentrations in mass and thickness, in obtaining broadband absorbers with a reduced thickness, in the range of 8.0 – 10.0 GHz , with superior attenuation of – 10 dB, that is, 90% absorption of incident radiation.

5. References

1. Srinivasamurthy KM, Angadi V J, Kubrin SP, Matteppanavar S, Sarychev DA, Kumar PM, et al. Tuning of ferrimagnetic nature and hyperfine interaction of Ni2+ doped cobalt ferrite nanoparticles for power transformer applications. Ceram Int. 2018;44(8):9194-203.

2. Patel J, Parekh K, Upadhyay RV. Performance of Mn-Zn ferrite magnetic fluid in a prototype distribution transformer under varying loading conditions. Int J Therm Sci. 2017;114:64-71.

3. Sai Ram B, Paul AK, Kulkarni SV. Soft magnetic materials and their applications in transformers. J Magn Magn Mater. 2021;537:168210.

4. Yang Y, Li J, Zhang H, Li J, Xu F, Wang G, et al. Nb[5+] ion substitution assisted the magnetic and gyromagnetic properties of NiCuZn ferrite for high frequency LTCC devices. Ceram Int. 2022;48(9):12490-6.

5. Yahui JL, Sun QL. Enhanced FMR linewidth and magnetic properties of In[3+]-doped YIG ferrite materials for microwave devices applications. J Magn Magn Mater. 2021;538:1.

6. Hasan IH, Hamidon MN, Ismail A, Ismail I, Mohd Azhari NA, Mohd Kusaimi MA, et al. Nickel zinc ferrite thick film with linseed oil as organic vehicle for microwave device applications. Mater Chem Phys. 2019;27:121790.

7. Nasrin S, Chowdhury F-U-Z, Hoque SM. Study of hyperthermia temperature of manganese-substituted cobalt nano ferrites prepared by chemical co-precipitation method for biomedical application. J Magn Magn Mater. 2019;479:126-34.

8. Jayababu S, Inbasekaran M, Narayanasamy S. Promising solar photodegradation of RY 86 by hydrophilic F127 (pluronic) aided nano cobalt ferrite and its biomedical applications. J Mol Liq. 2022;350:1.

9. Amiri M, Salavati-Niasari M, Akbari A. Magnetic nanocarriers: evolution of spinel ferrites for medical applications. Adv Colloid Interface Sci. 2019;265:29-44.

10. Wang Y, Miao Y, Fan H. Engineering ferrite nanoparticles with enhanced magnetic response for advanced biomedical applications. Mater Today. 2020;8:100119.

11. Kumar A, Sarbjit T, Singh SG. Investigation of the magnetic behavior of the ferrites of alkali and alkaline earth metals for biomedical application. Mater Today. 2021;36:621-5.

12. Xiong Y, Luo H, Nie Y, Chen F, Dai W, Wang X, et al. Synergistic effect of silica coated porous rodlike nickel ferrite and multiwalled carbon nanotube with improved electromagnetic wave absorption performance. J Alloys Compd. 2019;802:364-72.

13. Zhang N, Liu X, Huang Y, Wang M, Li S, Zong M, et al. Novel nanocomposites of cobalt ferrite covalently-grafted on graphene by amide bond as superior electromagnetic wave absorber. J Colloid Interface Sci. 2019;540:218-27.

14. Du H, Ai M, Lyu S-S, et al. Systematic fabrication and electromagnetic performance of porous biomass carbon/ferrite nanocomposites. J Alloys Compd. 2022;896:163048.

15. Derakhshani M, Taheri-Nassaj E, Jazirehpour M, Masoudpanah SM. Enhanced electromagnetic wave absorption performance of Ni–Zn ferrite through the added structural macroporosity. J Mater Res Technol. 2022;16:700-14.

16. Wang S-F, Chiang Y-J, Hsu Y-F, Chen C-H. Effects of additives on the loss characteristics of Mn–Zn ferrite. J Magn Magn Mater. 2014;365:119-25.

17. Jiang K, Li K, Peng C, Zhu Y. Effect of multi-additives on the microstructure and magnetic properties of high permeability Mn–Zn ferrite. J Alloys Compd. 2012;541:472-6.

18. Zapata A, Herrera G. Effect of zinc concentration on the microstructure and relaxation frequency of Mn–Zn ferrites synthesized by solid state reaction. Ceram Int. 2013;39(7):7853-60.

19. Arshad MI, Hasan MS, Rehman AU, Akhtar M, Tung LD, Amin N, et al. Structural, optical, electrical, dielectric, molecular vibrational and magnetic properties of La^{3+} doped Mg–Cd–Cu ferrites prepared by Co-precipitation technique. Ceram Int. 2022;48(10):14246-60.

20. Vadivelan S, Sowmiya S. Structural and magnetic studies of nickel doped barium ferrite via Co-Precipitation method. Physics. 2021;9:100094.

21. Ajeesha TL, Manikandan A, Anantharaman A, Jansi S, Durka M, Almessiere MA, et al. Structural investigation of Cu doped calcium ferrite ($Ca_{1-x}Cu_xFe_2O_4$; x = 0, 0.2, 0.4, 0.6, 0.8, 1) nanomaterials prepared by co-precipitation method. J Mater Res Technol. 2022;18:705-19.

22. Tanveer M, Nisa I, Nabi G, Khalid Hussain M, Khalid S, Qadeer MA. Sol-gel extended hydrothermal pathway for novel Cd-Zn co-doped Mg-ferrite nano-structures and a systematic study of structural, optical and magnetic properties. J Magn Magn Mater. 2022;553:169245.

23. Mhamad SA, Ali AA, Mohtar SS, Aziz F, Aziz M, Jaafar J, et al. Synthesis of bismuth ferrite by sol-gel auto combustion method: impact of citric acid concentration on its physico chemical properties. Mater Chem Phys. 2022;282:125983.

24. Kotru S, Paul R, Jaber AQ. Synthesis and magnetic studies of pure and doped NiZn ferrite films using Sol gel method. Mater Chem Phys. 2022;276:125357.

25. Manjunatha HC, Vidya YS, Damodara Gupta PS. Photocatalytic, shielding and cytotoxic properties of reduced graphene oxide and Barium Ferrite nanocomposite synthesized via green combustion method. Journal of Science: Advanced Materials and Devices. 2022;3:00442.

26. Martinson KD, Belyak VE, Sakhno DD, Ivanov AA, Lebedev LA, Nefedova LA, et al. Solution combustion assisted synthesis of ultra-magnetically soft LiZnTiMn ferrite ceramics. J Alloys Compd. 2022;894:162554.

27. Wang Q, Shen Z, Sun J, Shu C-M, Jiang J, Deng J, et al. Combustion characteristics of zirconium particles coated with ferrite nanoparticles. Powder Technol. 2021;389:145-54.

28. Santos RLP, Tavares MM, Cornejo DR, Kiminami RHGA, Costa ACFM. Comparative analysis of sintering Mn$_{0.65}$Zn$_{0.35}$Fe$_2$O$_4$ ferrite by microwave energy and N2 Atmosphere. Mater Sci Forum. 2012;727-728:1272-7.

29. Sun C, Cheng C, Sun M, Zhang Z. Facile synthesis and microwave absorbing properties of LiFeO2/ZnFe2O4 composite. J Magn Magn Mater. 2019;482:79-83.

30. Feng H, Huang J, Wang X, Li J, Yin X, Xu Z, et al. Microstructure and enhanced electromagnetic wave absorbing performance of Zn$_{0.6}$Ni$_{0.3}$Cu$_{0.1}$Fe$_2$O$_4$ ferrite glass-ceramic. Ceram Int. 2022;48(7):9090-8.

31. Ye Z, Wang K, Li X, Yang J. Preparation and characterization of ferrite/carbon aerogel composites for electromagnetic wave absorbing materials. J Alloys Compd. 2022;893:162396.

32. Yoo J-E, Kang Y-M. Electromagnetic wave absorbing properties of Ni-Zn ferrite powder–epoxy composites in GHz range. J Magn Magn Mater. 2020;513:167075.

33. Houbi A, Aldashevich ZA, Atassi Y, Bagasharova Telmanovna Z, Saule M, Kubanych K. Microwave absorbing properties of ferrites and their composites: a review. J Magn Magn Mater. 2021;529:167839.

34. Kumar S, Kumar P, Verma V. Electromagnetic interference shielding behaviors of in-situ polymerized ferrite-polyaniline nano-composites and ferrite-polyaniline deposited fabrics in X-band frequency range. J Alloys Compd. 2021;862:158331.

35. Dawei U, Chen Z, Jing O. Interfacial multi-reflection in barium ferrite nanosheets/ amorphous carbon nanotube composites for effective electromagnetic shielding applications. Mater Chem Phys. 2021;267:124606.

36. Silva VA, Pereira JJ, Nohara EL, Rezende MC. Comportamento eletromagnético de materiais absorvedores de micro-ondas baseados em hexaferrita de Ca modificada com íons CoTi e dopada com La. J Aerosp Technol Manag. 2009;1(2):255-63.

37. Ahmed I, Khan AN, Jan R, Gul IH. Structure: properties relationships of graphene and spinel nickel ferrites based poly(vinylidene fluoride) hybrid polymer nanocomposites for improved dielectric and EMI shielding characteristics. Mater Res Bull. 2022;148:111687.

38. Ali NN, Al-Qassar Bani Al-Marjeh R, Atassi Y, Salloum A, Malki A, Jafarian M. Design of lightweight broadband microwave absorbers in the X-band based on (polyaniline/MnNiZn ferrite) nanocomposites. J Magn Magn Mater. 2018;453:53-61.

39. Sharif A, Mustaqeem M, Saleh TA, ur Rehman A, Ahmad M, Warsi MF. Synthesis, structural and dielectric properties of Mg/Zn ferrites -PVA nanocomposites. Mater Sci Eng. 2022;280:115689.

40. Zhang X, Yi J, Yin Y, Song Y, Xiong C. Thermal conductivity and electrical insulation properties of h-BN@PDA/silicone rubber composites. Diamond Related Materials. 2021;117:108485.

41. Iacob M, Tiron V, Cazacu M. Bentonite as an active natural filler for silicone leading to piezoelectric-like response material. J Mater Res Technol. 2022;17:79-94.

42. Jain SR, Adiga KC, Verneker VP. A new approach to thermochemical calculations of condensed fuel-oxider mixture. Combust Flame. 1981;40:71-9.

43. Costa ACFM, Kiminami RHGA. Dispositivo para produção de nanomateriais cerâmicos em larga escala por reação de combustão e processo contínuo de produção dos nanomateriais. BR 10 2012 002181-3. 2012.

44. Chen Q, Li L, Wang Z, Ge Y, Zhou C, Yi J. Synthesis and enhanced microwave absorption performance of CIP@ SiO$_2$@Mn$_{0.6}$Zn$_{0.4}$Fe$_2$O$_4$ ferrite composites. J Alloys Compd. 2019;779:720-7.

45. Nakamura T, Tsutaoka T, Hatakeyama K. Frequency dispersion of permeability in ferrite composite materials. J Magn Magn Mater. 1994;138(3):319-28.

46. Qu F, Morais PC. An oxide semiconductor nanoparticle in an aqueous medium: a surface charge density investigation. J Phys Chem B. 2000;104(22):5232-6.

47. Yao C, Shimada Y, Muroga S, Qin GW, Okamoto S, Kitakami O, et al. High permeability and electromagnetic noise suppression characteristics of Fe–B–P sub-micron particle chains and their composites with NiZn–ferrite nanoparticles. J Alloys Compd. 2013;554:414-418.

48. Huang X, Chen J, Zhang J, Wang L, Zhang Q. A new microwave absorber based on antimony-doped tin oxide and ferrite composite with excellent electromagnetic match. J Alloys Compd. 2010;506(1):347-50.

49. Xu R, Wang LS, Liu XL, Lei M, Guo HZ, Chen Y, et al. Influence of substrate temperature on high-frequency soft magnetic properties of [Fe80Ni20–O/NiZn–ferrite]n multilayer thin films. J Alloys Compd. 2014;604:43-4.

50. Nasir S, Saleemi AS, Fatima-tuz-Zahra, Anis-ur-Rehman M. Enhancement in dielectric and magnetic properties of Ni–Zn ferrites prepared by sol-gel method. J Alloys Compd. 2013;572:170-174.

51. Zheng Z, Zhang H, Yang Q, Jia L. Structure and electromagnetic properties of NiZn spinel ferrite with nano-sized ZnAl2O4 additions. J Alloys Compd. 2015;648:160-7.

52. Ahmad M, Ali I, Grössinger R, Kriegisch M, Kubel F, Rana MU. Effects of divalent ions substitution on the microstructure, magnetic and electromagnetic parameters of Co2W hexagonal ferrites synthesized by sol–gel method. J Alloys Compd. 2013;579:57-645.

53. Collin RE. Foundations for microwave engineering. New York: John Wiley & Sons; 2001. 924 p.

54. Cohn Z, Daly J, Parker C. Advanced ferrite materials for anechoic chambers. Ceram Trans. 1995;47:269-84.